

Accepted Manuscript

Effect of curing cycle on void distribution and interlaminar shear strength in polymer-matrix composites

S. Hernández, F. Sket, J.M. Molina-Aldareguía, C. González, J. LLorca

PII: S0266-3538(11)00164-3
DOI: [10.1016/j.compscitech.2011.05.002](https://doi.org/10.1016/j.compscitech.2011.05.002)
Reference: CSTE 4982

To appear in: *Composites Science and Technology*

Received Date: 17 March 2011
Revised Date: 29 April 2011
Accepted Date: 8 May 2011



Please cite this article as: Hernández, S., Sket, F., Molina-Aldareguía, J.M., González, C., LLorca, J., Effect of curing cycle on void distribution and interlaminar shear strength in polymer-matrix composites, *Composites Science and Technology* (2011), doi: [10.1016/j.compscitech.2011.05.002](https://doi.org/10.1016/j.compscitech.2011.05.002)

This is a PDF file of an unedited manuscript that has been accepted for publication. As a service to our customers we are providing this early version of the manuscript. The manuscript will undergo copyediting, typesetting, and review of the resulting proof before it is published in its final form. Please note that during the production process errors may be discovered which could affect the content, and all legal disclaimers that apply to the journal pertain.

Effect of curing cycle on void distribution and interlaminar shear strength in polymer-matrix composites

S. Hernández¹, F. Sket¹, J. M. Molina-Aldareguía¹,
C. González^{1,2}, J. LLorca^{*,1,2}

¹ *Madrid Institute for Advanced Studies of Materials (IMDEA Materials Institute)
C/ Profesor Aranguren s/n. 28040 - Madrid, Spain.*

² *Department of Materials Science, Polytechnic University of Madrid and
CISDEM, UPM-CSIC
E. T. S. de Ingenieros de Caminos. 28040 - Madrid, Spain.*

Abstract

The effect of temperature cycle on the void volume fraction, shape and spatial distribution was determined by means of X-ray microtomography in [0]₁₀ AS4/8552 composite laminates manufactured by compression molding. Cure temperatures were designed to obtain different processing windows while the overall degree of cure was equivalent, leading to laminates with average porosities in the range 0.4 and 2.9 %. Regardless of the final porosity, voids were elongated, oriented parallel to the fibers and concentrated in channels along the width of the laminate as a result of the inhomogeneous process of consolidation and resin flow along the fibers. The interlaminar shear strength was found to be controlled by the void volume fraction in panels with porosity above 1%.

Key words: A. Polymer-matrix composites, B. Curing, B. Fracture, B. Porosity/voids, X-ray microtomography

Introduction

Fiber-reinforced polymer-matrix composites are nowadays extensively used in structural elements due to their high specific stiffness and strength. For high-performance components, manufacturing is carried out using prepreg laminas, which are stacked (either manually or with an automatic lay-up machine) and consolidated under the simultaneous application of pressure and temperature in an autoclave. Autoclave pressure impedes the growth of voids or even leads

* Corresponding author.

Email address: javier.llorca@imdea.org (J. LLorca).

to the collapse of air bubbles, giving rise to materials with excellent mechanical properties and very low porosity, as required by aerospace and sports industries. However, this manufacturing route is expensive in terms of capital investment and processing time and it is not cost-effective for use in other industrial sectors. These limitations had acted as driving forces to look for alternative out-of-autoclave processing routes. They include, among others, the use of prepregs in a standard resin transfer molding process (Black, 2010), replacing pressurized gas by a high thermal inertia fluid to reduce the curing time (Griffiths and Noble, 2004), or the development of special low temperature cure prepregs able to be cured in standard ovens. These techniques are able to produce composite parts faster but it should be noted that they do not often achieve the mechanical properties obtained in autoclave due to the lower fiber content and to the presence of voids and pores.

The mechanics of prepreg compaction in autoclave was pioneered by Springer and co-workers (Loos and Springer, 1983; Tang et al., 1987) starting from the consolidation theory developed for soil mechanics (Terzaghi, 1943). These authors described the resin flow through the composite following Darcy's flow theory in a porous medium, and determined the laminate compaction sequence. The external pressure was first supported by the resin and, as bleeding progressed through the surfaces, pressure was transferred to the fiber bed. This process continued until the composite reached the maximum compaction of the reinforcement and all the extra resin was expelled. Air bubbles are always present in the raw prepreg due to deficient fiber impregnation and others arise on the lamina surface during the preparation of the laminate kit, leading to an initial void population that is subjected to the curing cycle. The stability of voids as a function of the temperature and pressure has been extensively studied by Kardos et al. (1986), who considered the effects of the resin viscosity and of the resin-void surface tension. They developed a model for void growth which was successfully applied to predicting the occurrence of voids in thermoset composite materials manufactured by liquid molding (Ledru et al., 2010), autoclave or vacuum bagging (Grunenfelder and Nutt, 2010). Although these models provide the essentials of the mechanics of void growth in a polymer blend, they are restricted to small spherical voids surrounded by a viscous resin. Their validity is not proven for long cylindrical voids in a viscous matrix surrounded by aligned fibers, the standard morphology observed in out-of-autoclave composites. In addition, although there are many papers in the open literature regarding the detrimental effect of voids on the mechanical performance of composites (Costa et al., 2001; Wisnom et al., 1996; Bowles and Frimpong, 1992), there is a lack of information regarding the influence of curing conditions on the actual volume fraction, shape and spatial distribution of voids within the laminate.

This investigation was conceived as a first attempt to assess the effect of curing cycle on the development of voids during consolidation of prepregs at low pres-

sure (2 bars) by hot pressing. To this end, panels were manufactured using four different curing cycles carefully designed following the rheological and thermal analysis of the raw prepregs. The void volume fraction, shape and spatial distribution were analyzed in detail by means of X-ray computed microtomography, which has been demonstrated to be a very powerful technique for analyzing the microstructural features of composites (Enfedaque et al., 2010; Centea and Hubert, 2011), and the results were discussed in the light of the processing conditions. Finally, the matrix-controlled mechanical properties of the panels were measured to close the loop and establish the relationship between processing conditions and mechanical performance.

2. Material

Unidirectional carbon/epoxy AS4/8552 prepreg sheets were purchased from Hexcel. 8552 epoxy resin is a blend of a high functionality epoxy resin TGMDA (Tetraglycidyl methylenedianiline), a lower functionality epoxy resin TGpAP (Triglycidyl p-aminofenol) and the amines 4,4'-diaminodiphenylsulfone (DDS) and 3,3'-diaminodiphenylsulfone as curing agents. The epoxy system has been modified by the supplier by the incorporation of thermoplastic particles in order to enhance the fracture toughness and the impact performance (Hexcel, 2010b). The carbon reinforcement used in the prepreg was a polyacrylonitrile (PAN) high strength carbon fiber, AS4 (Hexcel, 2010a), unidirectionally distributed within the epoxy matrix. The nominal prepreg areal weight was 194 g/m².

Square (300×300 mm²) panels following the [0]₁₀ stacking sequence and 2 mm nominal thickness were manufactured by hot pressing (Fontijne Grotnes LabPro400). The prepreg laminas were stacked unidirectionally and placed between polytetrafluoroethylene sheets for an adequate releasing after the consolidation. No previous vacuum debulking of the laminate prepreg kit was performed and a constant pressure of 2 bars was applied immediately after placing the kit between the press plates. Four curing cycles were applied based on the rheological behavior of the AS4/8552 raw composite prepreg.

3. Experimental Techniques

3.1 Rheology and Thermal Analysis

Rheological measurements under dynamic mode were performed using a parallel plate rheometer (AR200EX, TA Instruments) with disposable plates. A prepreg raw sample of 25 mm in diameter was placed between the plates of the rheometer and subjected to an oscillatory shear strain of known amplitude and frequency while imposing a specified temperature cycle. The dynamic viscoelastic response of the composite prepreg in terms of the storage and loss moduli, G' and G'' , respectively, is modified by the cross-linking reactions and the evolution of the complex viscosity η^* (modulus of real and imaginary

parts) can be determined as

$$\eta^* = \frac{|G' + iG''|}{\omega} \quad (1)$$

where ω is the frequency of the oscillatory strain.

Differential scanning calorimetry (DSC) was used to measure the degree of curing, α , and the glass transition temperature, T_g , of the composite panels. The calorimetric experiments were carried out using a modulated differential scanning calorimeter (MDSC Q200, TA Instruments). Raw prepreg samples (10 mg) were placed onto the Al pan of the DSC apparatus and subjected to the corresponding temperature cycle. After cooling down to room temperature, the specimens were reheated at 5°C/min in a modulated mode (amplitude ± 2 s and period 100 s) in order to obtain the residual reaction heat ΔH_{res} and the glass transition temperature T_g . Finally, the dynamic reaction heat, ΔH_{din} was obtained on different prepreg samples heated at 10°C/min up to 350°C. The final degree of curing of each sample was computed as Lee et al. (1982)

$$\alpha = 1 - \frac{\Delta H_{res}}{\Delta H_{total}} \quad (2)$$

where ΔH_{total} is the total reaction heat of AS4/8552 prepreg (which was assumed to be equivalent to the dynamic reaction heat ΔH_{din}). The final volume fraction of carbon fiber reinforcement was measured using thermogravimetric experiments performed in a vertical thermobalance (model Q50, TA Instruments). The prepreg samples were heated from room temperature up to 1000°C at 10°C/min using two working atmospheres: N₂ up to 500°C and laboratory air at higher temperature to measure mass loss associated with thermal degradation of the epoxy resin. The nominal fiber volume fraction of the composite panels was obtained from the densities of carbon (1.79 g/cm³) and epoxy resin (1.3 g/cm³) without considering the void volume fraction.

3.2 Mechanical Characterization

The interlaminar shear strength test according to ASTM D2344 standard was selected to assess the effect of porosity on the mechanical performance of the composite panels (Costa et al., 2001; Wisnom et al., 1996; Bowles and Frimpong, 1992). Prismatic [0]₁₀ specimens of 20×10×2 mm³ (length×width×thickness) were machined from the center of the composite panels and tested under three point bending with 10 mm of span. 5 tests were performed under stroke control at a crosshead speed of 1 mm/min using an electromechanical universal testing machine (Instron 3384) for each material. The load was continuously measured during the test with a 30 kN load cell (Instron). The maximum load, P_{max} , was used to compute the interlaminar shear strength (ILSS) according to

$$\tau_{ILSS} = \frac{3P_{max}}{4bh} \quad (3)$$

where b and h stand, respectively, for the width and depth of the beam cross section. The fracture surfaces of the tested coupons were examined by scanning electron microscopy (EVO MA15, Zeiss) to ascertain the dominant fracture mechanisms

3.3 X-ray Computed Microtomography

The distribution of voids in the raw preregs and in the consolidated laminates was studied by X-ray computed microtomography (Nanotom 160NF, Phoenix). The tomograms were collected at 50 kV and 350 μ A using a Mo target. The resolution of most of the measurements was set to 11 μ m/voxel but a few analyses were carried out with a resolution of 4 μ m/voxel. Prismatic samples of 20×20 mm² and 2 mm in thickness were extracted from the central part of the laminates for the tomographic inspections. Evaluation of the reconstructed volume focused on the void population. For that purpose, voids were extracted by identifying the voxels belonging either to a void or to the bulk composite material based on their grey level. The threshold used for void segmentation was based on the local variance method from Niblack applied to each slice, adapting the threshold according to the mean and standard deviation of the peak belonging to the composite material. A void was previously defined as the configuration of voxels sharing a common face, edge, or a corner. Only voids larger than 2x2x2 or more connected voxels were considered as smaller voids can be artifacts from noise and were neglected in this work. After the computer tomography reconstruction, the grey level images were first thresholded in order to extract the porosity inside the laminates. The quantitative values of the volume fraction, distribution and geometry of voids were obtained with a Matlab program from the binarized volumes.

4. Definition of Cure Cycles

The definition of the cure cycles was performed from the rheological behavior of the AS4/8552 prepreg under isothermal conditions. Isothermal viscosity profiles were generated at 5.5 Hz of frequency and a shear strain amplitude of 0.05% at dwell temperatures of 110, 120, 130, 160, 170 and 180°C. Storage and loss moduli were determined from the shear stress-time curves and the corresponding complex viscosity modulus was calculated according to equation (1). The results of the influence of temperature on the minimum complex viscosity, η_{min}^* and of the gelation time are plotted in Figure 1. The gel point was assumed to be reached when $\tan \delta = G''/G'$ was independent of ω (Flory, 1941). The prepreg behavior showed the competition between two main physical mechanisms. On the one hand, the viscosity decreased with temperature as a result of the higher mobility of the polymer chains. On the other hand,

cross-linking reactions are activated with temperature, leading to shorter gel times.

From the viewpoint of composite processing, low cure temperature (≈ 110 - 120°C) favors long processing windows for consolidation but the high viscosity of the resin hinders fiber impregnation. Moreover, it also makes it difficult to move and squeeze out of the panel the air bubbles within the prepreg as well as the air entrapped between prepreg plies. High cure temperature (≈ 160 - 180°C) (which is necessary to reach elevated glass transition temperatures, an important condition for many applications) leads to low viscosities in the resin but the gelation time is dramatically reduced. Therefore, the curing cycle should be designed in such a way that a minimum viscosity is attained during the minimum time necessary to allow the voids to move and bleed out or dissolve before gelation.

Based on these considerations, four curing cycles were used to manufacture the composite panels (Figure 2). Pressure was held constant and equal to 2 bars during the whole temperature cycle in all cases but the temperature profile was different for each cycle to ascertain its influence on the void volume fraction, shape and spatial distribution. The simplest cycle, C-1, consists of heating at a constant rate until 180°C and follows the recommendation of the prepreg manufacturer for autoclave cure (which is carried out under 8 bars of hydrostatic pressure). Cycle C-2 was similar to C-1 but the heating ramp was interrupted at 130°C and the prepreg was held at this temperature for 20 minutes. This modification was intended to maintain the material for longer time at a low viscosity level, so void diffusion and transport was easier. Finally, cycles C-3 and C-0 presented the same temperature ramp until 180°C . This initial flash temperature peak was intended to reduce the viscosity and facilitate the impregnation of fibers and the transport of voids. The temperature was immediately reduced after the peak to 130°C and 110°C , respectively, in the cycles C-3 and C-0, held at this temperature for 20 minutes and finally increased up to 180°C . All the heating and cooling ramps were carried out at the same rate of $10^\circ\text{C}/\text{min}$ and this value was selected based on preliminary rheological experiments. The evolution of the complex viscosity during each cycle is also plotted together with the temperature profile in Figure 2. They show that final gelation did not took place in any case before the maximum temperature of 180°C was attained for the second time, and this guarantees enough time for resin flow and void evacuation leading to panels with low porosity ($< 3\%$).

Differential scanning calorimetry was used to measure the residual heat of reaction, ΔH_{res} , the degree of cure, α , and the glass transition temperature, T_g , as indicated above. The results for each curing cycle are summarized in Table 1. The values of the final degree of cure and of the glass transition were very similar for all cycles and equivalent to other data reported in the

literature (Costa et al., 2005; Ersoy and Tugutlu, 2005; Ersoy et al., 2005). They should be understood as indicators of a high cross-linking degree reached by the thermoset resin during curing, which should lead to similar mechanical properties of the resin. The fiber volume fraction, V_f , obtained from the thermogravimetric analysis, was $\approx 59\%$ in all cases.

5. Results and Discussion

5.1 Void volume fraction, shape and spatial distribution

A X-ray microtomography section perpendicular to the fiber tows of the raw prepreg is shown in Figure 3. The fiber content in the prepreg is much lower than in the final laminate and the average distance between fiber tows was $804 \pm 120 \mu\text{m}$. Porosity within the prepreg was limited and it was mainly concentrated within the tows, although isolated rounded pores in the matrix were also found.

So far, experimental studies on processing-associated porosity in polymer-matrix composites were carried out from optical or scanning microscopy analysis of cross-sections. In order to understand the results that will be presented below, results provided by optical microscopy (OM) and X-ray computed tomography (XCT) were compared. Figure 4a shows a montage of ten optical micrographies of a cross-section perpendicular to the fibers of a panel manufactured with cure cycle C-1. Three well-defined regions can be distinguished in the OM picture: fiber-rich regions (light gray), resin-rich regions (in gray, normally located around the fiber tows and showing an undulated behavior along the laminate) and porosity (dark gray) which was sometimes filled with resin during polishing, hindering pore evaluation. The same cross-sectional area was measured by XCT with a resolution of $4 \mu\text{m}$ (Figure 4b) and $11 \mu\text{m}$ (Figure 4c). The void area fractions determined from these micrographs were 1.9% (OM), 2.1% (XCT, $4 \mu\text{m}$) and 2.0% (XCT, $11 \mu\text{m}$). The differences between OM and XCT arose mainly from the pores filled with resin during polishing while the void area fraction determined by XCT with $11 \mu\text{m}$ resolution was slightly lower than that measured with $4 \mu\text{m}$ because the smallest pores were not detected at lower resolution. Nevertheless, their overall contribution to the total area fraction was of the same order of error associated to the experimental measurement.

XCT allows the straightforward determination of the area fraction of pores along the fiber direction, a very time-consuming task with OM. For instance, the analysis of 1500 slices along the fiber direction showed that the porosity varied between 2.0% and 4.1%, the average being 2.9% in laminate C-1. The drawback of XCT slices is that it is not possible to distinguish between the resin matrix and the carbon fibers due to the similarities in the X-ray absorption coefficient of both materials. However, this limitation was overcome in the

present case because the microstructure remains relatively constant along the fiber direction. Thus, it was possible to enhance the microstructural features (i.e. emphasize the differences between matrix-rich and fiber-rich regions) by averaging the gray levels along the fiber direction over all the slices. The results are shown in Figures 4(d) and 4(e) for the XCT obtained with 4 μm and 11 μm resolution, respectively. Resin bands were clearly visible under these conditions and, in addition, it was possible to observe the regions where the pores were concentrated (marked by the ellipsoids). These observations seem to indicate that most of the porosity came from air entrapment between lamina during lay-up. Light gray areas surrounding the resin bands correspond to high fiber density regions (marked by rectangles) around the resin bands. This effect was observed in the XCT with both 4 μm and 11 μm resolution.

XCT with 11 μm resolution was used to obtain information about the void spatial distribution and shape within the panels, as shown in Figure 5a, in which carbon fibers and resins were set to semi-transparency to reveal the voids. Voids were elongated and with the major axis parallel to the fiber orientation (Z axis). Each individual void was fitted to an equivalent cylinder of elliptical section whose volume, centroid and moments of inertia were equal to those of the void. Figure 5b shows the voxel reconstruction of a typical void, where the rod-like shape is clearly visible, and the corresponding equivalent cylinder. Voids were closely aligned with the fiber direction and the maximum misalignment was below $\approx 1.5^\circ$ (angle between the fiber direction and the principal axis of the equivalent cylinder). Information about the void shape was obtained from the statistical analysis of the dimensions of the equivalent cylinders. The cross-section of voids perpendicular to the fiber direction (Z axis) was characterized by the flatness ratio, f , which stands for the ratio between the semiaxes of the ellipsoidal section, as shown in Table 2. $f \approx 1.5$, regardless of the cure cycle, and this result points to the dominant effect of the applied pressure on the transversal shape of the voids. More interesting is the analysis of the elongation factor, defined as the ratio between the major axis and the average transversal axis (average of the minor and medium axes), which is plotted in Figure 6 as a function of the void volume expressed in voxels. The results for all the cure cycles are consistent and the larger the void, the greater the elongation and this is indicative of two different void origins. The smaller ones, with more rounded shapes could come from internal voids within the prepreg, either present before the consolidation (gas bubbles from resin mixing operations, broken fibers) or generated by diffusion of water during the cure cycle. Long, elongated voids were the result of air entrapment and wrinkles created during lay-up. Interestingly, the evolution of the elongation with the void volume is grouped into two sets; laminates manufactured following cure cycles C-1 and C-2 present higher elongations (by a factor of 2) than those processed with cycles C-0 and C-3.

Panel examination after processing revealed resin bleeding on the faces per-

pendicular to the fiber direction but not on the faces parallel to the fibers. This fact indicates that resin flow was anisotropic and mainly occurred along the fiber direction, in agreement with the higher permeability factor in this direction. The dominant resin flow along the fibers led to the formation of a channel-type structure (also reported in previous studies (Loos and Springer, 1983; Tang et al., 1987)) and facilitated the transport and coalescence of voids along the fibers. In addition, the cross-section of the elongated voids was reduced as a result of the compaction pressure and many of them eventually collapsed, leading to panels with very low porosity.

The volume fraction of voids, V_f , was obtained directly from the tomograms by numerical integration of the individual volume of all the voids, and it is reported in Table 2. The composite panels manufactured following curing cycles C-0 and C-1 contained the highest volume fraction of pores (2.7% and 2.9%, respectively), while curing cycle C-2 led to the minimum residual porosity (0.4%). For discussion purposes, the dynamic viscosity profiles presented previously in Figure 2 are now re-plotted together in Figure 7 with a zoom-in of the low viscosity region -the processing window- where consolidation takes place to establish the connections between the processing conditions and void volume fraction and spatial distribution. Low viscosity values (in the range $3\text{--}5 \cdot 10^5 \text{ Pa s}$) were attained ten minutes after the beginning of cure and were maintained for another ten minutes in all cycles. The viscosity increased sharply afterwards for the cycle C-1, and the processing window of this cycle was the shortest one. The time available for migration and/or diffusion of the air bubbles was limited and this led to the panel with the highest volume fraction of voids. On the contrary, the lowest porosity was attained with the cure cycle C-2. The viscosity was reduced rapidly as from the beginning of the cure cycle and the low viscosity levels ($< 5.0 \cdot 10^5 \text{ Pa s}$) were maintained during 30 minutes up to the final gelation, facilitating the migration/diffusion of air bubbles. More difficult is the interpretation of the results associated with cycles C-0 and C-3. In both cases, a flashing temperature peak of 180°C was applied to reduce the initial viscosity, followed by a reduction to 110°C (C-0) or 130°C (C-3) to increase the processing window. The dynamic viscosity profiles (Figure 7) for both cycles were initially superposed and differed slightly afterwards. Cycle C-0, where the dwell temperature after the initial flash was only 110°C , presented higher viscosity during consolidation and a longer processing window (50 minutes up to gelation) as compared with cycle C-3 (40 minutes). Nevertheless, these differences led to noticeable changes in the porosity levels, showing that small variations in the processing conditions may lead to significant changes in the material.

X-ray tomograms (Figure 5) showed that the voids tended to be aligned in channels parallel to the fibers. In order to quantitatively evaluate this effect, the volume fraction of voids was integrated along the fiber (Z axis) and laminate thickness (X axis) to obtain the distribution of porosity along the width

of the laminate (Y axis). The result is plotted in Figure 8(a), which shows that the voids were not distributed homogeneously across the width of the laminate but were concentrated in sections which were distributed periodically along the laminate width. The porosity of these sections was much higher than the average and, for instance, cure cycle C-1 (with an average porosity of 2.9%) presented zones with porosities of up to 9% while other sections were almost free of voids ($< 1\%$). In addition, the average distance between the high-porosity regions, $\Delta\bar{d}$, (shown in Table 2) was determined from the average distance between the peaks in void volume fraction distribution along Y direction (Figure 8a). It was around 1 mm in all samples, which is of the same order as the average distance between fiber tows in the raw prepreg (Figure 3).

More detailed information about the actual location of the high porosity regions can be found in Figure 8(b), which shows the X-ray absorption of the composite panel along the fiber axis. This image was obtained by averaging the gray values of parallel tomograms along the Z axis and takes advantage of the concentration of voids in channels parallel to the fibers and of the differences in density (and, thus, in X-ray absorption) between voids, resin and fibers. Black zones stand for low density sections which contain very high porosity. White zones represent high fiber density sections while gray zones are either low fiber density or resin-rich regions. Porosity was mainly concentrated within resin-rich tubular cells, which were separated by a skeleton of fiber-rich zones. This peculiar distribution of the porosity within the laminate is the result of process of inhomogeneous consolidation. Upon the application of pressure, most of the load is transferred through a continuous skeleton of fiber-rich regions. The higher pressure in these regions leads to the migration of resin as well as voids into the cells formed by the skeleton. The pressure in these regions is lower, facilitating the nucleation and/or growth of voids. In addition, resin flow along the fibers facilitated the coalescence of voids, so the elongation factor of individual voids increased with its volume (Figure 6). This fact that the average distance between the high-porosity regions, $\Delta\bar{d}$, is similar to the average distance between fiber tows in the raw prepreg supports this mechanism of consolidation.

These observations are very relevant from the viewpoint of understanding and simulating of void formation, because most of the models for void nucleation and growth during cure of thermoset-based composites assumed that voids develop within an homogenous medium Loos and Springer (1983); Kardos et al. (1986); Grunenfelder and Nutt (2010). Nevertheless, Figure 8(b) clearly demonstrates that inhomogeneities resulting from the formation of preferential percolation paths for load transfer during consolidation may alter significantly the pressure distribution within the laminate and modify the volume fraction, size and spatial location of the voids. Finally, the porosity distribution through the thickness of the laminate (X axis) was also obtained from the tomograms and is plotted in Figure 9. The porosity was maximum in the middle and

minimum (and close to zero) near to the upper and lower surfaces. These facts, together with the bell shape of the porosity distribution, are indicative that the voids located near the surfaces migrated easily under the application of pressure.

5.2 Mechanical properties

It has been well established in previous studies that porosity leads to a marked reduction in the composite mechanical properties, particularly those dominated by the matrix behavior like the interlaminar shear strength and the transverse tensile strength Liu et al. (2006); Bowles and Frimpong (1992). Thus, cure cycles which lead to the minimum porosity should produce the best mechanical behavior and this hypothesis was tested by measuring the ILSS of the laminates processed with different cure cycles. The corresponding values of the ILSS are plotted in Figure 10 and were in broad agreement with the hypothesis: laminates with the highest porosity (C-0 and C-1) showed the lowest ILSS, while those with the minimum volume fraction of voids (C-1 and C-2) presented the highest ILSS. In addition, the relationship between ILSS and void volume fraction could be rationalized with a very simple model, which assumed that the cylindrical voids were arranged in a regular square pattern within the laminate. The drop in the ILSS due to reduction in the composite net section is given by

$$\tau_{ILSS}(V_f) = \tau_{ILSS}(0\%) \left[1 - \left(\frac{4V_f}{\pi} \right)^{1/2} \right] \quad (4)$$

where $\tau_{ILSS}(0\%)$ is the theoretical ILSS for the void-free laminate. This expression was fitted by the least squares method to the experimental results (leading to an ILSS for the void free laminate of 116 MPa) and it is plotted in Figure 10, together with the experimental data. Although the general trends were well captured by the net section analysis, the model overestimated the ILSS of the composite C-2 that presented the lowest void volume fraction (0.4%). This reduction in strength may be caused by a different factor because it was suggested that ILSS was insensitive to the void content below $\approx 1\%$ (Costa et al., 2001). The degree of curing α attained with the different cure cycles was very similar (see Table 1) and it was therefore expected that the shear strength of the epoxy matrix should be similar for all cure cycles.

In order to rationalize the behavior of the laminate processed following cycle C-2, the fracture surfaces of the ILSS coupons corresponding to laminates C-2 and C-3 were examined in the scanning electron microscope. Representative micrographs in Figure 11 show the typical cusp structures (platelets inclined on the surface), indicative of fracture by shear along the fiber direction Greenhald (2009). Cusps are formed as successive, parallel microcracks, initiated by shear in the epoxy matrix in front of the main crack tip at an angle of 45°

with the shear (fiber) direction. The microcracks propagate at this angle until they are stopped at the fiber-matrix interface and cusps are formed as the inclined microcracks coalesce along the main crack propagation direction. While the fracture micromechanisms were equivalent in both laminates, it is evident that the height and size of the cusps were larger in laminate C-3, and this is indicative of a tougher matrix, a stronger interface or a change in the coalescence mechanism due to the different shape of the voids, as indicated by the elongation factor (Figure 6) which was higher in laminate C-2.

In order to understand better the differences in ILSS and fracture morphology between laminates C-2 and C-3, a thorough micromechanical characterization of the resin and the matrix/fiber interface was performed by means of instrumented nanoindentation (Hysitron TI950). Nanoindentation tests with a pyramidal tip were carried out in appropriate areas of the laminate cross-sections where resin pockets were formed to study the matrix behavior. At least 10 indentations were performed in each sample with a maximum load of 0.7 mN. The hardness was quantified using the Oliver and Pharr (O&P) method Oliver and Pharr (1992) and the results are summarized in Table 3. Irrespectively of the appropriateness of the O&P method to calculate the hardness in polymers, the hardness of the resin after both curing cycles was the same, as expected from their identical degree of curing and glass transition temperature (see Table 1). This is also shown in Figure 12(a) in which two representative load-displacement curves were plotted (one for each laminate). The insert in Figure 12(a) corresponds to a scanning probe microscopy (SPM) image showing a resin pocket and the array of indentations performed. Only those indentations in the resin that were sufficiently far away from the surrounding fibers (further than 10 times the indentation depth, as a rule of thumb) were used to calculate the hardness in order to avoid any constrain effects induced by the fibers.

In the case of the interface strength, the differences were analyzed by means of push-in tests as it has been suggested that the cure cycle can modify this parameter Davies et al. (2007). Push-in tests are carried out by using a flat punch (with a diameter of $3.5\ \mu\text{m}$) to push individual fibers on the cross-section of a bulk specimen (Kalinka et al., 1997; Molina-Aldareguía et al., 2011) and offer the advantage this can be performed on actual laminates without complex sample preparation. The initial load-fiber displacement response is linear, Figure 12(b), corresponding to the elastic deformation of the fiber and the matrix, and it was shown that the departure from linearity at the critical load P_c coincides with the onset of interfacial debonding (Molina-Aldareguía et al., 2011). The actual value of the interface strength can be determined from P_c by taking into account the elastic properties of matrix and fibers as well as the constraining effect of the surrounding fibers. In the case of isotropic glass fibers, good results have been obtained through the application of the shear-lag model while more sophisticated computational analysis are required for

anisotropic materials (Molina-Aldareguía et al., 2011). In the particular case of the laminates considered here, the interfacial strength can be considered approximately proportional to the critical loads, which were identical and are marked with an arrow in the load-fiber displacement curves plotted in Figure 12(b). Up to 10 push-in tests were performed in each case and the average critical loads, reported in Table 3, indicate that the interfacial strength of laminates C-2 and C-3 was equivalent. Thus, neither the resin nor the interface strength can explain the slight differences in ILSS observed between the laminates manufactured following cure cycles C-2 and C-3, which were perhaps caused by the differences in the void morphology.

6. Conclusions

Unidirectional laminates of an AS4/8552 polymer matrix composite were manufactured by compression molding under 2 bars of pressure and different temperature cycles, which were designed according to the rheological and thermochemical behavior of the raw preregs. Similar degree of curing and glass transition temperature was achieved for all the cycles but the volume fraction of voids varied from 0.4% to 2.9%. Longer processing windows (more time before gelation) led to laminates with lower fraction of voids for simple temperature cycles (involving only ramps and holds). In the case of complex cycles, involving flash temperatures followed by holds at lower temperatures, the final void volume fraction also depended on the actual evolution of the dynamic viscosity throughout the cycle.

Void shape and spatial distribution was analyzed in detail by means of X-ray microtomography. Voids were elongated and the elongation factor (length/average diameter) increased with void size. Most of the voids were the result of air entrapment and wrinkles created during lay-up. They were oriented parallel to the fibers and concentrated in channels along the width of the laminate. Images obtained by integrating the gray values of parallel tomograms along the fiber axis showed a cellular structure with a cell diameter of the order of ≈ 1 mm. The cell walls were fiber-rich regions and porosity was localized at the center of the resin-rich cells. This peculiar distribution of the porosity within the laminate was the result of inhomogeneous consolidation. Upon the application of pressure, most of the load was transferred through a continuous skeleton of fiber-rich regions. The higher pressure in these regions led to the migration of resin as well as voids into the cells. In addition, the pressure within the cells was lower, facilitating the nucleation and/or growth of voids. Finally, resin flow along the fibers facilitated the coalescence of voids in this direction, so the elongation factor of individual voids increased with its volume. Finally, the effect of the cure cycle on the mechanical properties was assessed by means of ILSS tests. For void contents above 1%, the ILSS decreased with the void volume fraction according to the predictions of a simple net-section analysis, which assumed that the cylindrical voids were arranged in a regular

square pattern.

Acknowledgements This investigation was supported by the European project DEFCOM (EraNet MATERA) and by the Comunidad de Madrid through the program ESTRUMAT (S2009/MAT-1585). The authors would like to acknowledge the support of Dr. Dietmar Salaberger (Upper Austria University of Applied Sciences) in X-ray tomography and the comments and insights of Mrs. Marta Hortal and Prof. Peter Degischer (Vienna University of Technology) during the course of this investigation.

References

- Black, S., 2010. Same-qualified resin transfer molding. *High Performance Composites* September, 2010.
- Bowles, K., Frimpong, S., 1992. Voids effects on the interlaminar shear strength of unidirectional graphite-fiber-reinforced composites. *Journal of Composite Materials* 26, 1487–1509.
- Centea, T., Hubert, P., 2011. Measuring the impregnation of an out-of-autoclave prepreg by micro-ct. *Composites Science and Technology* 71, 593–599.
- Costa, M., Almeida, S., Cerqueira, M., 2001. The influence of porosity on the interlaminar shear strength of carbon/epoxy and carbon/bismaleimide fabric laminates. *Composite Science and Technology* 61, 2101–2108.
- Costa, M., Cocchieri, E., Faulstich, J., Cerqueira, M., 2005. Characterization of cure of carbon/epoxy prepreg used in aerospace field. *Materials Research* 8, 317–322.
- Davies, L., Day, R., Bond, D., Nesbitt, A., Ellis, J., Gardon, E., 2007. Effect of cure cycle heat transfer rates on the physical and mechanical properties of an epoxy matrix composite. *Composites Science and Technology* 67, 1892–1899.
- Enfedaque, A., Molina-Aldareguía, J. M., Gálvez, F., González, C., LLorca, J., 2010. Effect of glass-fiber hybridization on the behavior under impact of woven carbon fiber/epoxy laminates. *Journal of Composite Materials* 44, 3051–3068.
- Ersoy, N., Potter, K., Wisnom, M. R., Clegg, M. J., 2005. Development of spring-in angle during cure of a thermosetting composite. *Composites: Part A* 36, 1700–1706.
- Ersoy, N., Tugutlu, M., 2005. Cure kinetics modeling and cure shrinkage of a thermosetting composite. *Polymer engineering and Science* 50, 84–92.
- Flory, P. J., 1941. Molecular size distribution in three dimensional polymers. I. Gelation. *Journal of the American Chemical Society* 63, 3083–3090.
- Greenhald, E. S., 2009. *Failure Analysis and Fractography of Polymer Composites*. Woodhead Publishing Limited.

- Griffiths, B., Noble, N., 2004. Process and tooling for low cost, rapid curing of composites structures. *SAMPE Journal* 40, 41–46.
- Grunenfelder, L. K., Nutt, S. R., 2010. Void formation in composite prepregs effect of dissolved moisture. *Composites Science and Technology* 70, 2304–2309.
- Hexcel, 2010a. extow AS4 carbon fiber product data.
URL www.hexcel.com
- Hexcel, 2010b. Hexply 8552 epoxy matrix product data.
URL www.hexcel.com
- Kalinka, G., Leistner, A., Hampe, A., 1997. Characterisation of the fibre/matrix interface in reinforced polymers by the push-in technique. *Composites Science and Technology* 57, 845–851.
- Kardos, J. L., Dudukovic, M. P., Dave, R., 1986. Void growth and resin transport during processing of thermosetting matrix composite. *Advances in Polymer Science* 80, 101–123.
- Ledru, Y., Bernhart, G., Piquet, R., Schmidt, F., Michel, L., 2010. Coupled visco-mechanical and diffusion void growth modeling during composite curing. *Composites Science and Technology* 70, 2139–2145.
- Lee, W. I., Loos, A. C., Springer, G. S., 1982. Heat reaction, degree of cure and viscosity of Hercules 3501-6 resin. *Journal of Composite Materials* 16, 510–520.
- Liu, L., Zhang, B.-M., Wang, D.-F., Wu, Z.-J., 2006. Effects of cure cycles on void content and mechanical properties of composite laminates. *Composite Structures* 73, 303–309.
- Loos, A. C., Springer, G. S., 1983. Curing of epoxy matrix composites. *Journal of Composite Materials* 17, 135–169.
- Molina-Aldareguía, J. M., Rodríguez, M., González, C., LLorca, J., 2011. An experimental and numerical study of the influence of local effects on the application of the fibre push-in test. *Philosophical Magazine* 91, 1293–1307.
- Oliver, W. C., Pharr, G. M., 1992. A new improved technique for determining hardness and elastic modulus using load and sensing indentation experiments. *Journal of Materials Research* 7, 1564–1582.
- Tang, J.-M., Lee, W. I., Springer, G. S., 1987. Effects of cure pressure on resin flow, voids, and mechanical properties. *Journal of Composite Materials* 21, 421–440.
- Terzaghi, K., 1943. *Theoretical Soil Mechanics*. John Wiley & Sons.
- Wisnom, M. R., Reynolds, T., Gwilliam, N., 1996. Reduction in interlaminar shear strength by discrete and distributed voids. *Composite Science and Technology* 56, 93–101.

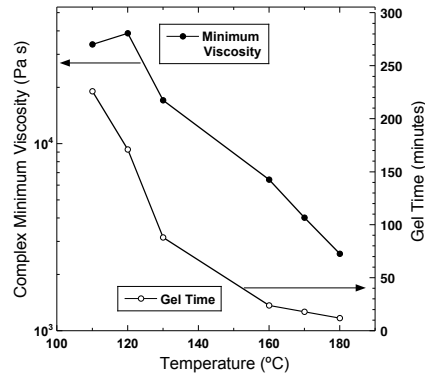


Fig. 1. Minimum complex viscosity η_{min}^* and gel time t_{gel} under isothermal conditions AS4/8552 prepreg.

Table 1

Residual heat of reaction, ΔH_{res} , degree of cure, α , and glass transition temperature, T_g of AS4/8552 composite panels manufactured with different curing cycles.

Cycle	ΔH_{res} (J/g)	α	T_g (°C)
C-1	19.1	0.891	207.6
C-2	18.4	0.895	210.4
C-3	18.3	0.896	210.6
C-0	15.7	0.910	211.9

Table 2

Volume fraction of voids, V_f , void flatness ratio, f , and average distance between sections with high porosity along the panel width (Y axis), $\Delta \bar{d}$, as a function of the cure cycle for AS4/8552 laminates.

Cycle	V_f (%)	f	$\Delta \bar{d}$ (μm)
C-1	2.9	1.45	973 ± 286
C-2	0.4	1.49	1075 ± 374
C-3	1.1	1.52	1276 ± 330
C-0	2.7	1.41	1131 ± 275

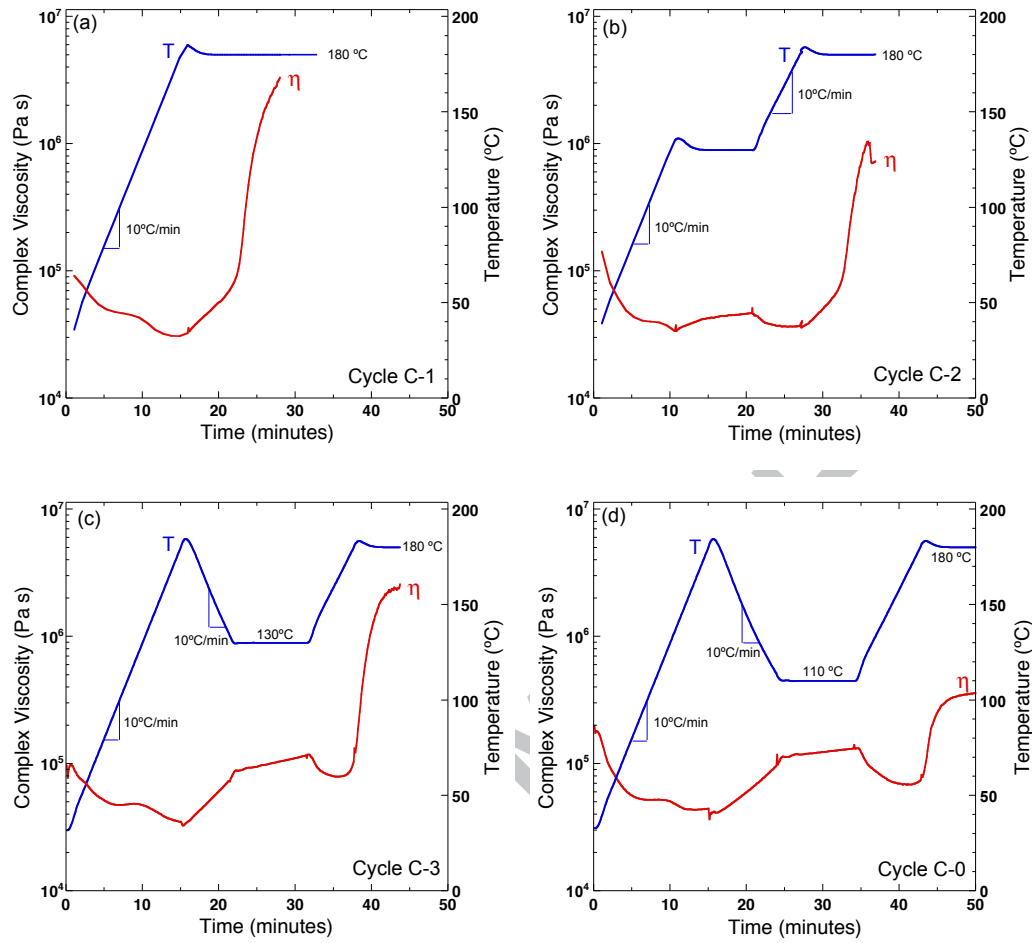


Fig. 2. Temperature cure cycles used to process AS4/8552 composite prepreg and the corresponding evolution of the complex viscosity η^* during the cycle. (a) cycle C-1; (b) cycle C-2; (c) cycle C-3; (d) cycle C-0.

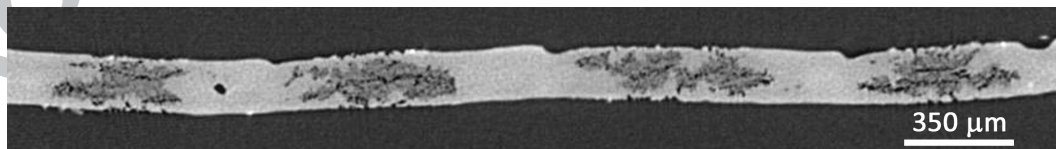


Fig. 3. X-ray microtomography of the raw prepreg cross-section perpendicular to the fiber tows. Matrix appears as light gray regions, fibers tows as dark gray regions and pores are black. Porosity was mainly concentrated within the tows although isolated, large pores were occasionally found in the matrix.

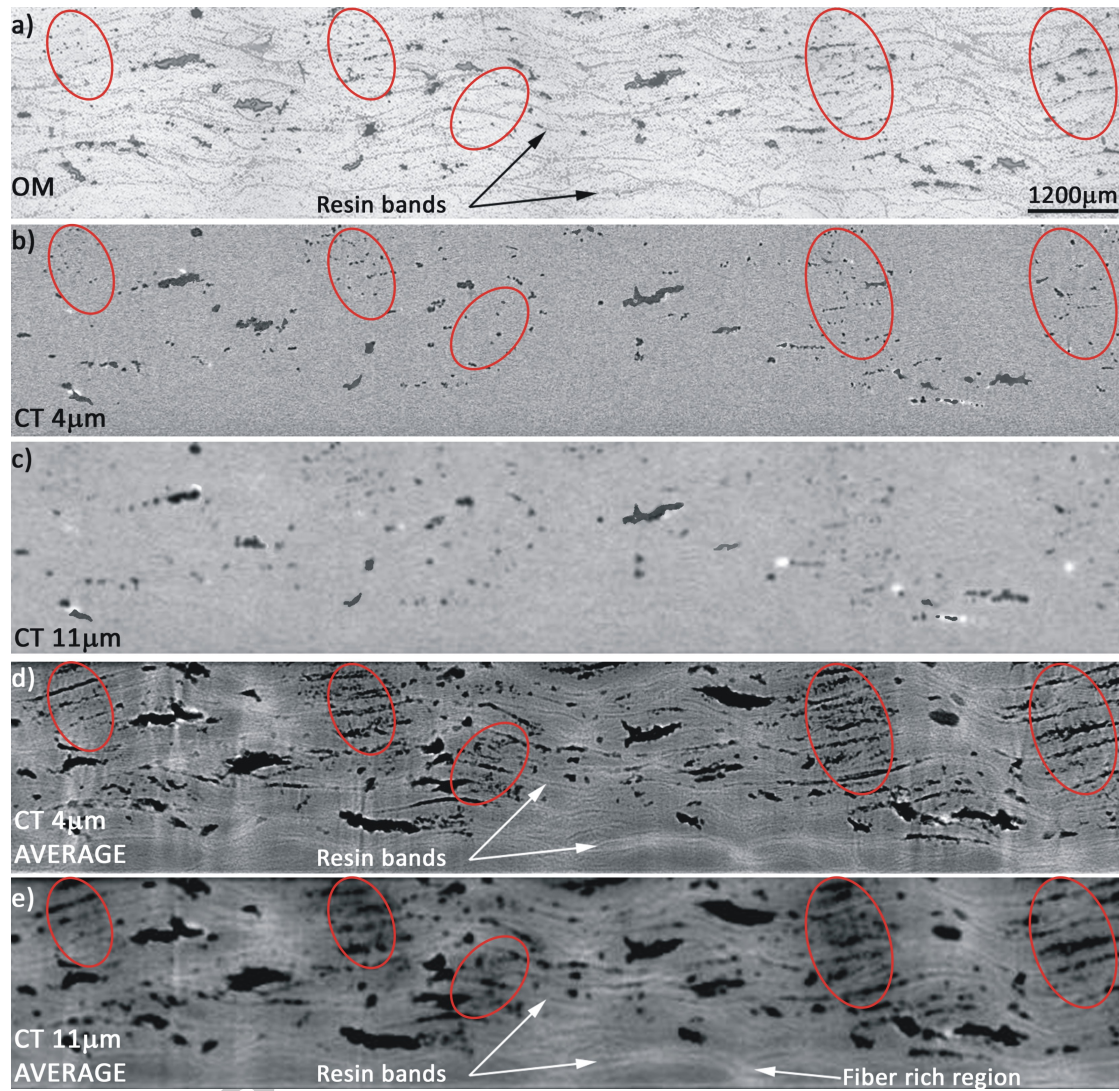


Fig. 4. (a) OM montage of a cross-section of the composite panel manufactured with cure cycle C-1. (b) XCT slice of the same cross-section with 4 μm resolution. (c) *Idem* as (b) with 11 μm resolution. (d) Average of the all slices along the fiber direction with 4 μm resolution. (e) *Idem* as (d) with 11 μm resolution. Regions with a large volume fraction of interply voids are marked with an ellipsoid.

Table 3

Resin hardness H and critical load for fiber-matrix interfacial debonding, P_c as determined from nanoindentation tests.

Cycle	H	P_c
	(MPa)	(mN)
C-2	410 ± 30	24 ± 2
C-3	420 ± 20	24 ± 1

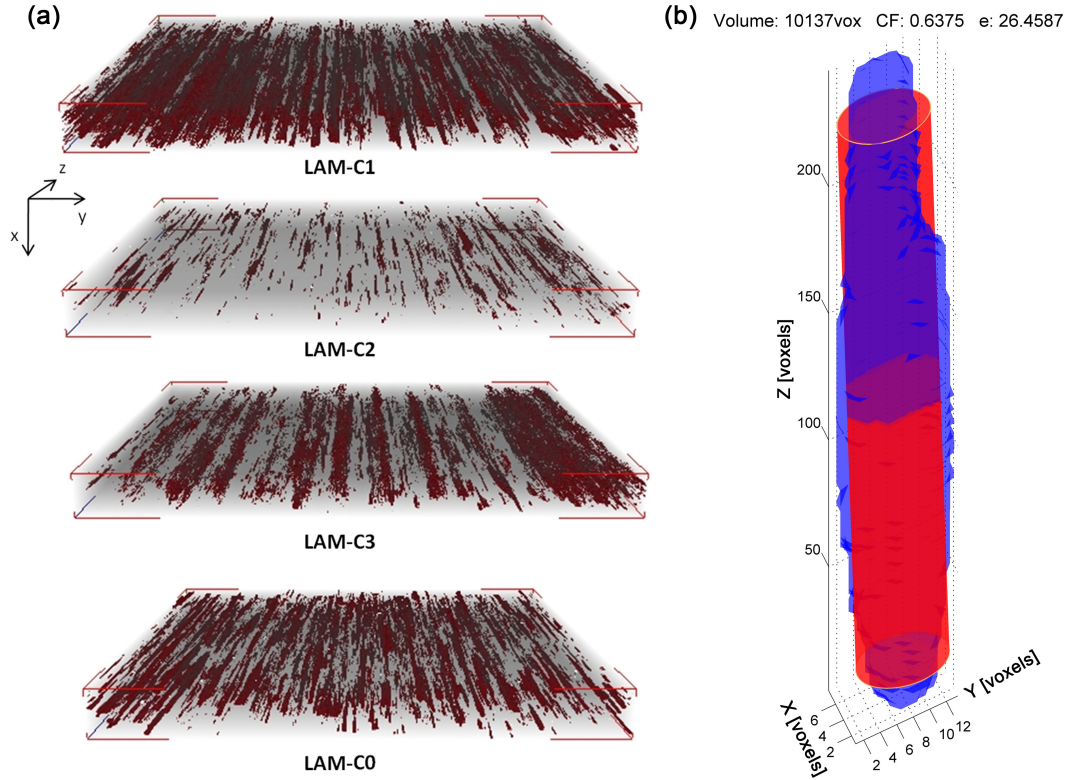


Fig. 5. (a) X-ray microtomography of void spatial distribution in the composite panels manufactured according to the curing cycles C-1, C-2, C-3 and C-0. (b) Typical rod-like void together with its equivalent cylinder.

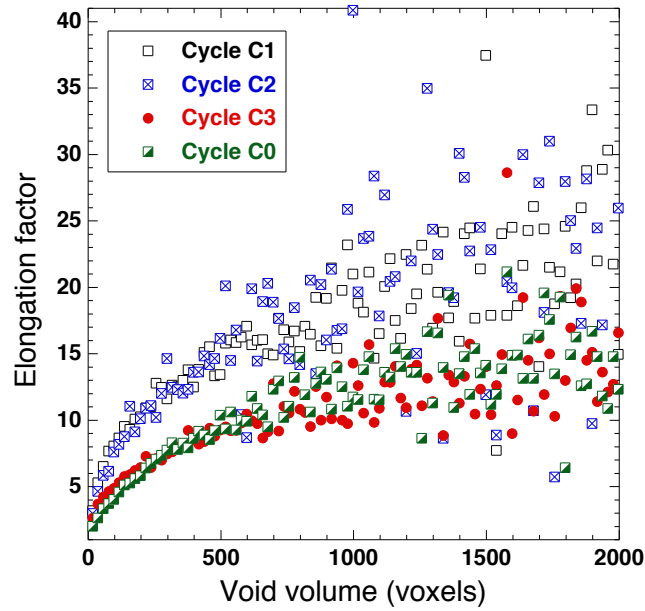


Fig. 6. Elongation factor of individual voids for the different cure cycles.

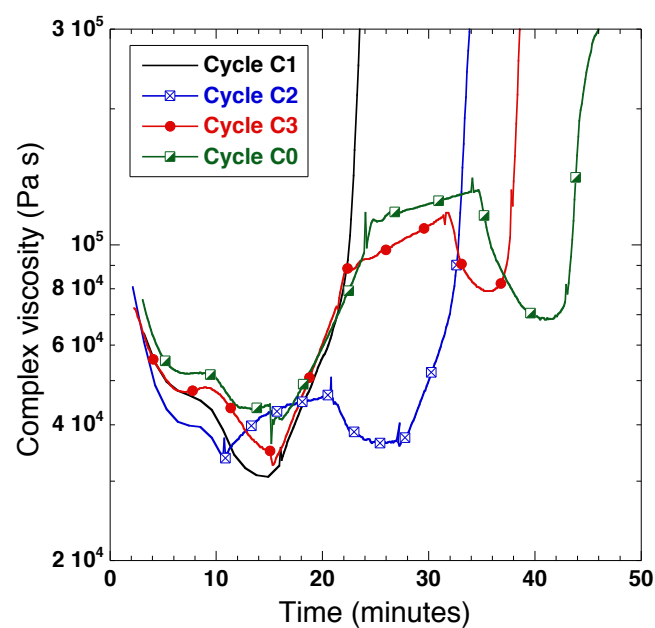


Fig. 7. Dynamic evolution of the complex viscosity η^* of AS4/8552 composite prepreg at the processing window region.

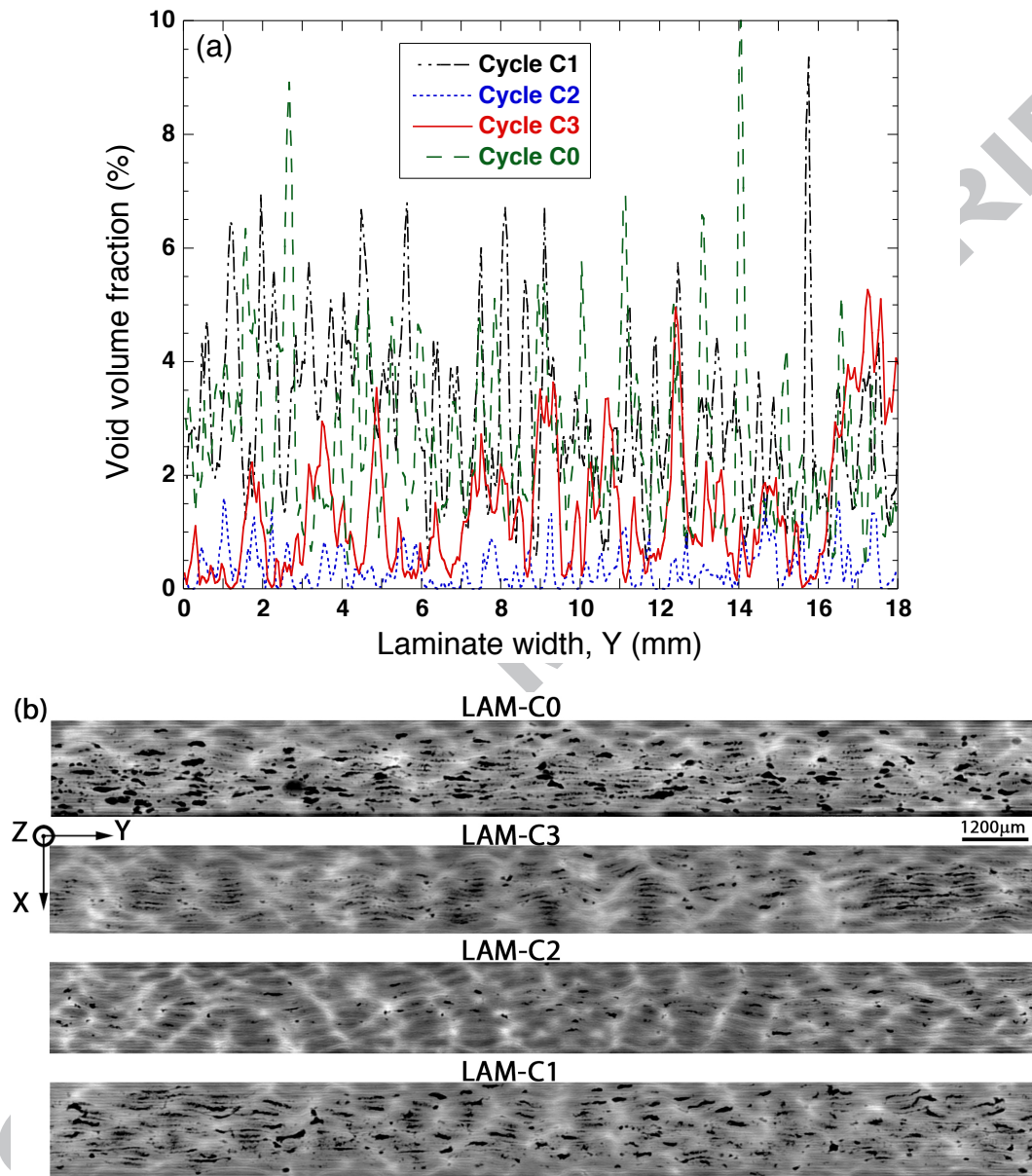


Fig. 8. (a) Distribution of porosity along the width (Y axis) of the laminates. (b) Average X-ray absorption of composite panel along the fiber (Z-axis). Black zones stand for low density sections (pores), while white zones represent high density sections (fibers). Gray zones stand for matrix-rich regions.

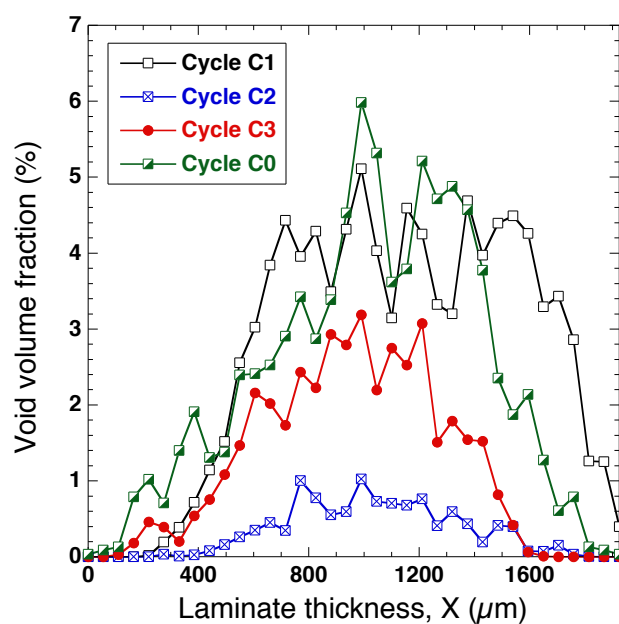


Fig. 9. Void distribution through the thickness of the laminate (X axis)

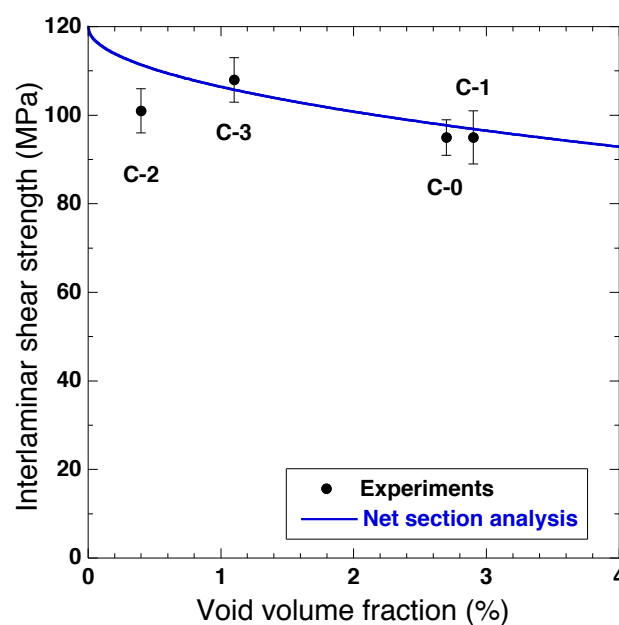


Fig. 10. Interlaminar shear strength of the AS4/8552 composite laminates as a function of void content.

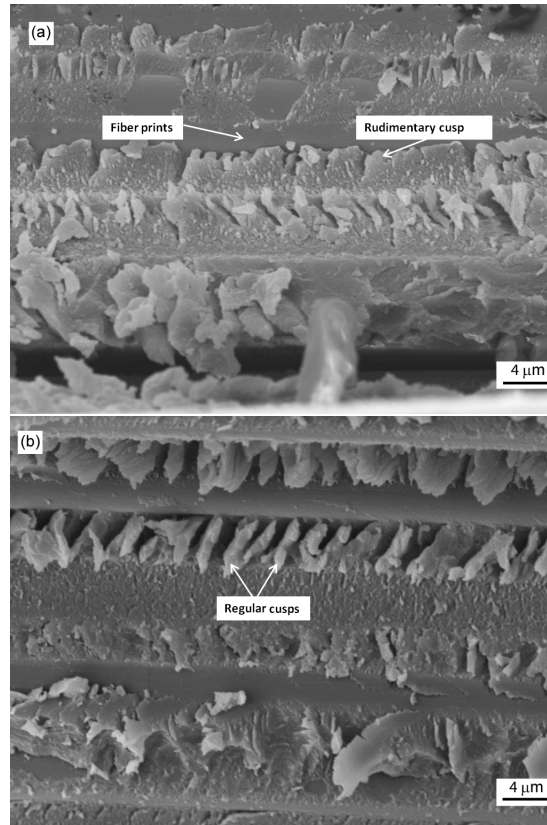


Fig. 11. Scanning electron micrographs of the fracture surfaces of coupons tested to measure the ILSS. (a) Cure cycle C-2. (b) Cure cycle C-3.

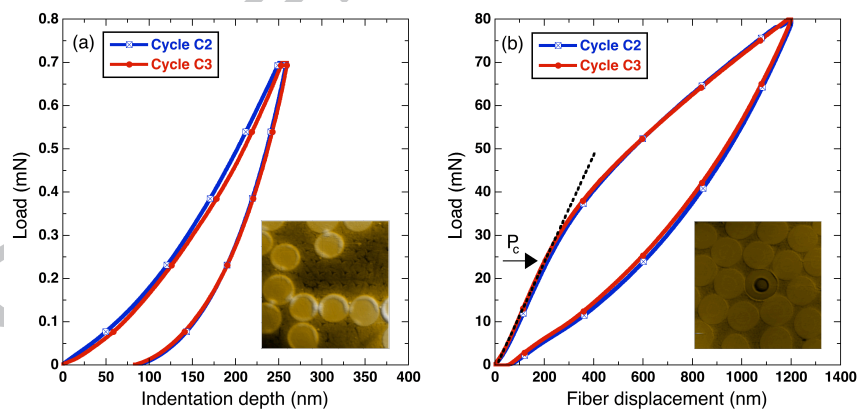


Fig. 12. (a) Load-indentation depth curves corresponding to pyramidal indentation tests of the resin processed with cure cycles C-2 and C-3, displaying identical behavior. An array of indentations in one of the resin pockets is shown in the 30x30 μm SPM image. (b) Load-fiber displacement curves corresponding to fiber push-in tests in laminates processed with cure cycles C-2 and C-3. The arrow indicates the critical load for interfacial debonding, which was the same in both cases. The insert corresponds to a 30x30 μm SPM image showing one fiber debonded from the matrix after the push-in test.